An Integral Boundary Layer Method using Discontinuous Galerkin Discretization and Captured Transition Modeling

Shun Zhang[*], Mark Drela[†], Marshall C. Galbraith[‡], Steven R. Allmaras[§], and David L. Darmofal[¶]
Massachusetts Institute of Technology, Cambridge, MA, 02139

Viscous analysis is crucial for understanding aerodynamic performance metrics such as profile drag. For three-dimensional (3D) viscous analysis, Reynolds-averaged Navier-Stokes (RANS) solvers are often the fastest available tool in practice but the required computational efforts preclude its extensive use for preliminary design. In contrast, the integral boundary layer (IBL) method offers a computationally more efficient alternative with comparable effectiveness when applicable. However, existing IBL methods mostly rely on two-dimensional (2D) or quasi-2D assumptions and thus remain to be extended to a fully 3D formulation for general configurations. To this end, we continue the development of an IBL method with discontinuous Galerkin (DG) finite element discretization and strong viscous-inviscid coupling. The current work proposes a captured laminar-to-turbulent flow transition treatment for the IBL method that can be more conveniently extended to the 3D case compared to a previously examined fitted transition approach. The current captured transition treatment also leverages a more robust nonlinear solution method and achieves accurate solution of transitional flows. Moreover, correction to the standard DG discretization is introduced for well-behaved numerical solution. Numerical results of the proposed method in a 2D implementation compares well with XFOIL and demonstrate its capability for practical aerodynamic analysis with free transition.

Nomenclature

$\mathbf{r}$	position vector		x, y	global Cartesian coordinates
$\mathbf{q}$	velocity vector		ξ	local surface coordinate
q	speed $(= |\mathbf{q}|)$		$\hat{\mathbf{e}}$	local Cartesian basis vector
ρ	density		$s, \hat{\mathbf{s}}_1$	streamwise coordinate, basis vector
$\boldsymbol{\tau}$	shear stress vector		$\widetilde{\nabla}(\cdot)$	$\partial(\cdot)/\partial\xi\, \hat{\mathbf{e}}$
$\mathcal{D}$	dissipation integral		$()_{\mathrm{i}}$	equivalent inviscid flow (EIF) quantity
δ^*	mass defect thickness		$()_{\mathrm{e}}$	viscous layer edge quantity
θ	momentum defect thickness		$()_{\mathrm{w}}$	wall quantity
θ^*	kinetic defect thickness		$()_{\infty}$	freestream quantity
H	shape parameter $H = \delta_1^*/\theta_{11}$		$\widehat{()}$	unit vector
H^*	kinetic energy shape parameter $H^* = \theta_1^*/\theta_{11}$		$\overline{\overline{()}}$	tensor

Scalars are in normal font, vectors are boldface, and tensors are boldface with double overbars. Other notations follow the nomenclature used in Ref. [1] or will be defined later where they first appear.

I. Introduction

Computational fluid dynamics (CFD) has become a powerful and indispensable tool for aerodynamic design and analysis. For lack of faster and cheaper options that effectively capture the important viscous effects, the current common practice of three-dimensional (3D) viscous aerodynamic analysis predominantly relies on CFD algorithms based on

---

[*]Graduate Research Assistant, Department of Aeronautics & Astronautics, AIAA Student Member
[†]Terry J. Kohler Professor, Department of Aeronautics & Astronautics, AIAA Fellow
[‡]Research Engineer, Department of Aeronautics & Astronautics, AIAA Member
[§]Research Engineer, Department of Aeronautics & Astronautics, AIAA Associate Fellow
[¶]Professor, Department of Aeronautics & Astronautics, AIAA Associate Fellow

solving the Reynolds-averaged Navier-Stokes (RANS) equations. However, the computational efforts (including setup and solution) to obtain RANS solution remains overwhelmingly high for extensive use in preliminary aerodynamic design, which generally sets the aerodynamic shape and thus plays a key role in the overall aircraft design. The preliminary design stage requires exploration of the design space through numerous design iterations but under a restrictive budget. Hence, it calls for analysis methods with fast speed, low cost and reasonable modeling capability (including capturing viscous aerodynamic effects).

Throughout the past decades, two-dimensional (2D) viscous aerodynamic design and analysis has in fact benefited tremendously from the integral boundary layer (IBL) methods for its rapid computational speed. For example, XFOIL computes an entire drag polar for an airfoil within a few seconds [2] and able to achieve comparable or even better solution accuracy compared to RANS solvers, especially in cases with flow transition [3]. Moreover, in fluid-structure interaction (FSI) problems, the aerostructural coupling is more conveniently realized using a displacement body model in the IBL formulation [4] in contrast to mesh movement algorithms required for RANS methods [5]. Given its rapid speed, modeling capability and multi-disciplinary compatibility, the IBL method is well suited for medium-fidelity aerodynamic and aeroelastic analysis in preliminary design.

Despite successful two-dimensional (2D) examples of the IBL method such as MSES [6] and XFOIL [2], however, a counterpart of comparable capability and reliability for three-dimensional (3D) applications is not yet available. The quasi-2D method, such as Boeing's proprietary TRANAIR code [7–9], provides an intermediate solution but falls short in fully 3D cases. On the other hand, traditional 3D boundary layer solvers depend on explicit curvilinear coordinates and are thus limited to simple geometries. This issue can be sidestepped by finite element IBL formulations [1, 10–14] which are applicable to general 3D configurations. Strong viscous-inviscid coupling is also a key ingredient for robust IBL methods [2, 6] and Refs. [1, 13] provide a strong coupling scheme that allows for a flexible choice of the inviscid solver and potential extension to aerostructural coupling.

Extending Ref. [14], the current work develops a robust discontinuous Galerkin (DG) discretization for the IBL equations and a captured transition treatment that can be readily extended to general 3D cases. The transition treatment is able to utilize more robust nonlinear solution methods and to resolve flow transition accurately. This paper focuses on evaluating the capability of aerodynamic analysis of free transition and uses the example of a coupled 2D IBL formulation, while the proposed methodology is designed to conveniently generalize to the 3D case.

The following sections describe the viscous-inviscid formulation, the numerical discretization scheme, and the strongly-coupled viscous-inviscid solution procedure. Numerical results of the proposed method are presented on selected airfoil test cases to demonstrate the capability of aerodynamic analysis with free transition.

II. Integral Boundary Layer Formulation

This section briefly summarizes a 2D incompressible integral boundary layer formulation of which the detailed theory (including notation and derivation) was presented in Refs. [1, 14]. Additions and modifications are elaborated in this paper which are intended to be readily generalizable to 3D boundary layers.

A. Governing Equations

The governing equations are mass and momentum conservation laws,

$$\frac{\partial \rho}{\partial t} + \nabla \cdot (\rho \, \mathbf{q}) = 0 \qquad \text{(mass)} \tag{1}$$

$$\frac{\partial (\rho \, \mathbf{q})}{\partial t} + \nabla \cdot (\rho \, \mathbf{q} \otimes \mathbf{q}) + \nabla \cdot \left(p \, \bar{\bar{\mathbf{I}}} - \bar{\bar{\boldsymbol{\tau}}} \right) = \mathbf{0} \qquad \text{(momentum)} \tag{2}$$

Forming $\left\{ 2\mathbf{q} \cdot [\text{equation (2)}] - q^2 \, [\text{equation (1)}] \right\}$ yields the following kinetic energy equation,

$$\frac{\partial (\rho \, q^2)}{\partial t} + \nabla \cdot \left(\rho \, q^2 \, \mathbf{q} \right) + 2\mathbf{q} \cdot \left[\nabla \cdot \left(p \, \bar{\bar{\mathbf{I}}} - \bar{\bar{\boldsymbol{\tau}}} \right) \right] = 0 \qquad \text{(kinetic energy)} \tag{3}$$

These equations apply to both viscous and inviscid flows, albeit the viscous stress tensor $\bar{\bar{\boldsymbol{\tau}}}$ vanishes in the inviscid case.

By subtracting the viscous equations from the inviscid equations, integrating them across the thickness of the shear layer, and applying thin shear layer approximations, the following integral defect equations are derived (as done in detail

in Ref. [1]),

$$\frac{\partial m}{\partial t} + \widetilde{\nabla} \cdot \mathbf{M} - \rho_e \, \mathbf{q}_e \cdot \hat{\mathbf{n}}_w = 0 \qquad \text{(mass)} \qquad (4)$$

$$\frac{\partial \mathbf{p}}{\partial t} + m \frac{\partial \mathbf{q}_e}{\partial t} + \widetilde{\nabla} \cdot \overline{\overline{\mathbf{P}}} + \left(\widetilde{\nabla} \mathbf{q}_e \right) \cdot \mathbf{M} - \boldsymbol{\tau}_w = \mathbf{0} \qquad \text{(momentum)} \qquad (5)$$

$$\frac{\partial k}{\partial t} + m \frac{\partial \left(q_e^2 \right)}{\partial t} + \widetilde{\nabla} \cdot \mathbf{K} + \mathbf{D} \cdot \widetilde{\nabla} \left(q_e^2 \right) - 2 \, \mathcal{D} = 0 \qquad \text{(kinetic energy)} \qquad (6)$$

Eqs. (5) and (6) form the IBL equations, whereas Eq. (4) specifies the wall transpiration boundary condition for the outer inviscid flow in viscous-inviscid interaction.

The edge velocity $\mathbf{q}_e$ (of magnitude q_e) is governed by the inviscid flow. Integral defect quantities, the wall shear stress vector $\boldsymbol{\tau}_w$, and the dissipation integral $\mathcal{D}$ are defined in the same manner as Ref. [1],

$$
\begin{aligned}
m &\equiv \int (\rho_i - \rho) \, \mathrm{d}n & &= \rho_e \, \delta_\rho & &\text{mass defect} \\
\mathbf{M} &\equiv \int (\rho_i \, \mathbf{q}_i - \rho \, \mathbf{q}) \, \mathrm{d}n & &= \rho_e \, \delta^* \, \mathbf{q}_e & &\text{mass defect flux} \\
\mathbf{p} &\equiv \int \rho \, (\mathbf{q}_i - \mathbf{q}) \, \mathrm{d}n & &= \mathbf{M} - m \, \mathbf{q}_e & &\text{momentum defect} \\
\overline{\overline{\mathbf{P}}} &\equiv \int \rho \, (\mathbf{q}_i - \mathbf{q}) \otimes \mathbf{q} \, \mathrm{d}n & &= \rho_e \, \theta \, \mathbf{q}_e \otimes \mathbf{q}_e & &\text{momentum defect flux (tensor)} \\
\overline{\overline{\mathbf{J}}} &\equiv \int (\rho_i \, \mathbf{q}_i \otimes \mathbf{q}_i - \rho \, \mathbf{q} \otimes \mathbf{q}) \, \mathrm{d}n & &= \overline{\overline{\mathbf{P}}} + \mathbf{q}_e \otimes \mathbf{M} & &\text{momentum flux defect (tensor)} \\
k &\equiv \int \rho \, (q_i^2 - q^2) \, \mathrm{d}n & &= \rho_e \, \theta_0^* \, q_e^2 & &\text{kinetic energy defect} \\
\mathbf{K} &\equiv \int \rho \, (q_i^2 - q^2) \, \mathbf{q} \, \mathrm{d}n & &= \rho_e \, \theta^* \, q_e^2 \, \mathbf{q}_e & &\text{kinetic energy defect flux} \\
\mathbf{D} &\equiv \int (\rho_i - \rho) \, \mathbf{q} \, \mathrm{d}n & &= \rho_e \, \delta^{**} \, \mathbf{q}_e & &\text{density defect flux} \\
\mathcal{D} &\equiv \int \left(\overline{\overline{\boldsymbol{\tau}}} \cdot \nabla \right) \cdot \mathbf{q} \, \mathrm{d}n & &= \rho_e \, q_e^3 \, C_{\mathcal{D}} & &\text{dissipation integral} \\
\boldsymbol{\tau}_w &\equiv \overline{\overline{\boldsymbol{\tau}}} \cdot \hat{\mathbf{n}}_w & &= \frac{1}{2} C_{f_1} \, \rho_e \, q_e \, \mathbf{q}_e & &\text{wall shear stress}
\end{aligned}
\qquad (7)
$$

Based on the first-order boundary layer theory adopted in the current formulation, the inviscid velocity $\mathbf{q}_i$ is constant within the boundary layer and equal to the edge velocity $\mathbf{q}_e$. The density defect flux $\mathbf{D}$ vanishes for incompressible flows.

The solution variables are chosen to be displacement and momentum defect thicknesses, i.e. $\{\delta^*, \theta\}$ respectively. Together with $\mathbf{q}_e$, they close the integral defect equations (1), (2) and (3) through the following parameters and closure relations,

$$Re_\theta \equiv \frac{\rho_e \, q_e \, \theta}{\mu_e}, \qquad H \equiv \frac{\delta^*}{\theta}, \qquad H^* \equiv \frac{\theta^*}{\theta} = H^*(H, Re_\theta), \qquad C_{f_1} = C_{f_1}(H, Re_\theta), \qquad C_{\mathcal{D}} = C_{\mathcal{D}}(H, Re_\theta) \qquad (8)$$

the full expressions of which follow Ref. [15].

B. Flow Transition Modeling

An e^N envelope method is adopted for modeling laminar-to-turbulent flow transition. The method is based on the Orr-Sommerfeld linear flow stability theory, and captures natural transition by monitoring the growth of the Tollmien-Schlichting (TS) waves. Fig. 1 illustrates the notional evolution of flows undergoing transition within a boundary layer. The maximum magnitude of TS waves is characterized by the magnitude q' of the velocity fluctuation $\mathbf{q}'$ from the Reynolds decomposition and relates to the small Reynolds stress in the laminar regime.

In the standard e^N envelope method, the amplification factor $\tilde{n} \equiv \ln(q'/q_0')$ is defined as the natural exponent of the amplification ratio, where the initial disturbance level q_0' is governed by the boundary layer's receptivity to the background flow. The evolution of $\tilde{n}$ is driven by the following transport equation,

$$\frac{\partial \tilde{n}}{\partial t} + \mathbf{q}_e \cdot \widetilde{\nabla} \tilde{n} - \frac{q_e}{\theta} f_N + (1 - R) \frac{1}{t_{\text{ref}}} \exp\left(-\frac{q_e^2}{q_{\text{ref}}^2} \right) (\tilde{n} - \tilde{n}_0) = 0 \qquad (9)$$
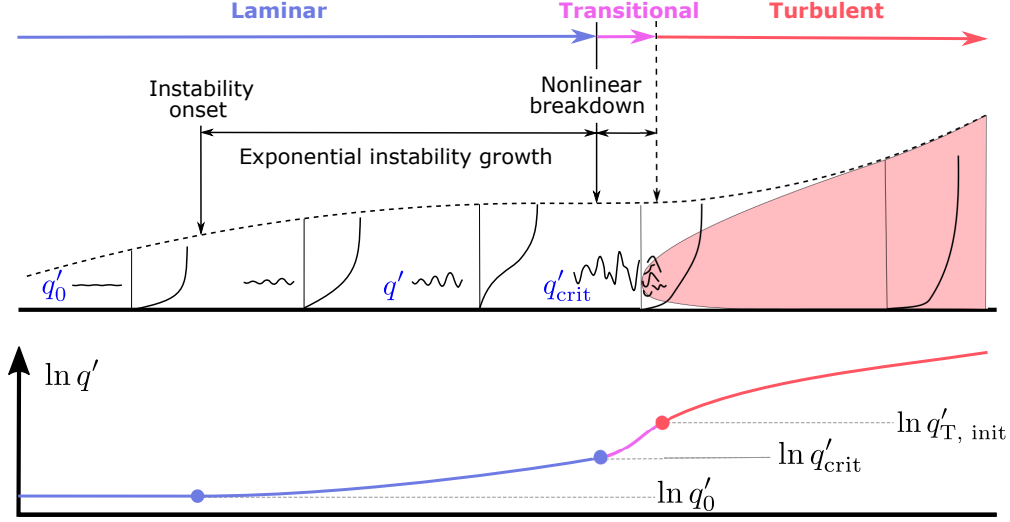
3

Fig. 1 Laminar-to-turbulent flow transition in a generic boundary layer (top) and the corresponding evolution of the Reynolds velocity fluctuation q' in the natural logarithmic scale (bottom). (The size of the transitional flow region is exaggerated in this figure, but flow transition is assumed to occur instantaneously, corresponding to effectively a step jump of the magenta curve.) Reproduced from Ref. [14] with permission.

The forcing function f_N drives the growth of $\tilde{n}$. The ramp function R models the onset of TS wave amplification; specifically, R is effectively zero and one, respectively, before and after the instability onset. The value of $\tilde{n}$ at the flow stagnation location (where $q_e = 0$) is $\tilde{n}_0 = 0$, corresponding to the initial disturbance level q'_0 of the background flow. The condition $\tilde{n} = \tilde{n}_0$ is weakly enforced by a source term in Eq. (9) to avoid the need of explicitly identifying the stagnation location. The following parameters and closure relations are adopted,

$$f_N = f_N(H; Re_\theta), \qquad R = R(H; Re_\theta), \qquad t_{\text{ref}} = \frac{\theta^2 \rho_e}{\mu_e}, \qquad q_{\text{ref}} = q_\infty \qquad \text{(laminar)} \qquad (10)$$

Full expressions of $f_N(H; Re_\theta)$ and $R = R(H; Re_\theta)$ are given in Ref. [14]. They are formulated for laminar flows but do not have to be defined for turbulent flows if a fitted transition treatment such as those of Refs. [14, 15] is adopted. In favor of an alternative transition treatment, the current formulation extends the amplification factor equation (9) to the turbulent regime by introducing the following definitions,

$$f_N = K_N \left(\tilde{n}_{\text{crit}} - \tilde{n}_0 \right) \frac{\theta}{c}, \qquad R = 1 \qquad \text{(turbulent)} \qquad (11)$$

where K_N is a non-dimensional parameter and c is a characteristic length scale over which the shear layer develops. In the airfoil test cases, for example, c is chosen as the chord length and $K_N = 4$ is a practical value correspondingly. The turbulent f_N is intended to maintain the growth of $\tilde{n}$ in the turbulent flows. Re-laminarization is not considered at present although it can potentially be modeled by modifying the turbulent function f_N. With the extension to turbulent flows, Eq. (9) is defined in the entire flow domain as a separate equation in the IBL formulation, and can also be readily applied to a general 3D formulation.

The nonlinear breakdown to transition is assumed to trigger as soon as the amplification factor $\tilde{n}$ reaches some critical threshold $\tilde{n}_{\text{crit}}$ corresponding to q'_{crit}. Such process, if any, is assumed to occur so rapidly over an infinitesimally small transitional region and effectively demarcates laminar and turbulent flows; that is,

$$\tilde{n} < \tilde{n}_{\text{crit}} \rightarrow \text{laminar}, \qquad \tilde{n} \geq \tilde{n}_{\text{crit}} \rightarrow \text{turbulent} \qquad \text{(transition criterion)} \qquad (12)$$

We note that the transition criterion (12) is based on the amplification factor $\tilde{n}$ instead of the absolute magnitude of q', and the value of $\tilde{n}_{\text{crit}}$ reflects the background flow fluctuation level q'_0 in comparison to q'_{crit}.

Forced transition is allowed with an additional criterion that flow transition can be triggered at a prescribed trip location. Bypass and cross-flow transition mechanisms can also be incorporated into the current e^N envelope method by enriching the definition of f_N (as in Refs. [12, 16]) without altering the overall transition treatment and are not considered in this paper.

4

C. Turbulent Dissipation Closure and Shear Stress Transport

The turbulent dissipation closure model follow Ref. [14], in which the dissipation coefficient $C_{\mathcal{D}}$ is given by,

$$C_{\mathcal{D}} = \frac{C_{f_1}}{2} U_{\mathrm{s}} + C_\tau (1 - U_{\mathrm{s}}) \tag{13}$$

The normalized apparent wall slip velocity is denoted by U_{s}, and the non-dimensional coefficient $c_\tau \equiv \tau/(\rho_{\mathrm{e}} q_{\mathrm{e}}^2) \approx q'^2/q_{\mathrm{e}}^2$ characterizes the Reynolds shear stress that dominates the dissipation effect in the outer layer. An alternative variable $\mathcal{G}$ is defined as $\mathcal{G} \equiv \ln(q'/q_{\mathrm{e}}) = \ln\left(c_\tau^{1/2}\right)$. The evolution of $\mathcal{G}$ is governed by the lag equation as follows to account for the lag effect in the turbulent shear stress transport,

$$\frac{\partial \mathcal{G}}{\partial t} + \mathbf{q}_{\mathrm{e}} \cdot \widetilde{\nabla}\mathcal{G} - \frac{q_{\mathrm{e}}}{2\,\widetilde{\delta}}\left[5.6\left((c_\tau)_{\mathrm{eq}}^{1/2} - c_\tau^{1/2}\right)\right] - \frac{q_{\mathrm{e}}}{B_{\mathrm{eq}}\delta_1^*}\left[\frac{C_{f_1}}{2} - \left(\frac{H-1}{A_{\mathrm{eq}}K_{\mathrm{dl}}H}\right)^2\right] + \widetilde{\nabla}\cdot\mathbf{q}_{\mathrm{e}} = 0 \tag{14}$$

Full expressions of the following parameters and closure relations were provided in Ref. [14],

$$U_{\mathrm{s}} = U_{\mathrm{s}}(H, Re_\theta), \qquad \widetilde{\delta} = \widetilde{\delta}(\theta, H), \qquad (c_\tau)_{\mathrm{eq}} = (c_\tau)_{\mathrm{eq}}(H, Re_\theta), \qquad \left\{K_{\mathrm{dl}}, A_{\mathrm{eq}}, B_{\mathrm{eq}}\right\} \tag{15}$$

For free wakes, the skin friction coefficient C_{f_1} is set to zero and the turbulent dissipation closure (13) corresponds to a half wake and is doubled to account for the entire viscous layer.

The shear stress magnitude from the outset of turbulent viscous layer, corresponding to $q'_{\mathrm{T, init}}$ as shown in Fig. 1, is specified as follows,

$$c_\tau = (c_\tau)_{\mathrm{T, init}} = \left(1.8\exp\left(-\frac{3.3}{H-1}\right)\right)^2 (c_\tau)_{\mathrm{eq}}, \qquad \mathcal{G}_{\mathrm{T, init}} = \frac{1}{2}\ln\left[(c_\tau)_{\mathrm{T, init}}\right] \qquad \text{(turbulent outset)} \tag{16}$$

This turbulent initial condition needs to be enforced at the transition front which constitutes a free-moving interface in the interior of the overall physical domain under consideration and thus poses challenges on the numerical discretization [14]. One workaround is to extend the lag equation to the laminar regime as follows,

$$\frac{\partial \mathcal{G}}{\partial t} + \mathbf{q}_{\mathrm{e}} \cdot \widetilde{\nabla}\mathcal{G} - K' K_G \left(\mathcal{G}_{\mathrm{T, init}} - \mathcal{G}\right)\frac{1}{t_{\mathrm{ref}}} = 0 \qquad \text{(laminar)} \tag{17}$$

where the non-dimensional parameter K_G is chosen to be positive and large so that $\mathcal{G}$ follows $\mathcal{G}_{\mathrm{T, init}}$ closely as they both evolve. For example, $K_G = 10$ is a practical choice. The non-dimensional parameter K' is defined as,

$$K' = \min\left\{1, \exp\left(\frac{\mathcal{G}_{\mathrm{T, init}} - \mathcal{G}}{\mathcal{G}_{\mathrm{ref}}}\right)\right\}, \qquad \mathcal{G}_{\mathrm{ref}} = 0.05 \tag{18}$$

so that $\mathcal{G}$ will not decrease excessively after it surpasses $\mathcal{G}_{\mathrm{T, init}}$ from below. With the laminar extension given by Eq. (17), the value of $\mathcal{G}$ is driven to approximately reach $\mathcal{G}_{\mathrm{T, init}}$ at transition and thus satisfies the turbulent initial condition (16).

The lag equation, a combination of Eqs. (14) and (17), stands as a fourth equation in the current IBL formulation, in addition to Eqs. (5), (6) and (9). Its extension to the entire flow domain sidesteps the need of explicitly imposing the interface condition (16) at the free-moving transition front. Hence, it significantly simplifies the modeling of free transition and can also be easily generalized to the 3D case.

III. Numerical Discretization

This section describes the numerical discretization of the IBL equations. The current IBL formulation is conducive to the standard discontinuous Galerkin (DG) finite element discretization, albeit with proper tailoring of the numerical flux in accordance with fundamental conservation laws. In addition, a numerical intermittency factor is introduced to regularize the discontinuity arising in the IBL equations with transition modeling.

A. Discontinuous Galerkin Formulation

The 2D steady-state IBL equations without unsteady terms are discretized using the DG FEM for manifold partial differential equations (PDEs) presented in Ref. [1].

The computational domain identified with the open set Ω is discretized into a triangulation $\mathcal{T}_h$ comprised of disjoint open finite elements K such that

$$\overline{\Omega} = \bigcup_{K \in \mathcal{T}_h} \overline{K} \tag{19}$$

The DG finite element solution space is

$$\mathcal{V}_h \equiv \left\{ v_h \in L^2(\Omega) : v_h|_K \in \mathcal{P}^p(K), \ \forall K \in \mathcal{T}_h \right\} \tag{20}$$

where $\mathcal{P}^p(K)$ denotes the space of polynomials that have a degree up to p and are restricted to the element K. Let $\{\mathcal{W}_j\}$ ($j = 1, 2, \ldots$) be a complete set of basis functions of $\mathcal{V}_h$ that are locally supported on finite elements and discontinuous across element boundaries. The DG approximation of the primary unknowns $\boldsymbol{v}$ is

$$v_h|_K (\xi) = \sum_j v_{h,j} \, \mathcal{W}_j(\xi) \qquad \forall K \in \mathcal{T}_h \tag{21}$$

Similar to the solution discretization, the shape of the triangulation $\mathcal{T}_h$ as defined by the position vector $\mathbf{r}|_K$ is approximated as

$$\mathbf{r}_h|_K (\xi) = \sum_j \mathbf{r}_{h,j} \, \mathcal{W}_j(\xi) \qquad \forall K \in \mathcal{T}_h \tag{22}$$

The local basis vector of an element K is conveniently constructed as a unit vector tangent to the element,

$$\hat{\mathbf{e}} \equiv \frac{\partial \mathbf{r}_h / \partial \xi}{\|\partial \mathbf{r}_h / \partial \xi\|}, \qquad \frac{\partial \mathbf{r}_h}{\partial \xi} = \sum_j \mathbf{r}_{h,j} \frac{\partial \mathcal{W}_j}{\partial \xi} \tag{23}$$

which is allowed to be discontinuous across finite element interfaces.

Let each of the scalar IBL equations (including the scalar component of Eq. (5) along $\hat{\mathbf{e}}$) be cast into a generic form of first-order PDE as follows,

$$\widetilde{\nabla} \cdot \mathbf{F}(v) + S(v) = 0 \tag{24}$$

Then, the discrete equation in a standard DG formulation is,

$$\mathcal{R}_{\text{IBL}} (v_h, \mathcal{W}) \equiv \sum_{K \in \mathcal{T}_h} \int_K \left(\mathcal{W} S(v_h) - \widetilde{\nabla} \mathcal{W} \cdot \mathbf{F}(v_h) \right) \mathrm{d}\ell + \sum_{\partial K \in \partial \mathcal{T}_h} \mathcal{W} \hat{\mathbf{t}} \cdot \widehat{\mathbf{F}}(v_h) = 0, \qquad \forall \mathcal{W} \in \mathcal{V}_h \tag{25}$$

where $\partial \mathcal{T}_h$ denotes the set of all the element boundaries ∂K, and $\widehat{\mathbf{F}}(v_h)$ is the numerical flux to be defined in Sec. III.B. Additional matching conditions are treated following Ref. [14], including mass and momentum conservation conditions at any joint between boundary layers and free wakes.

B. Numerical Flux

The numerical flux $\widehat{\mathbf{F}}(v_h)$ in Eq. (25) remains to be defined. A straightforward option is a fully upwinded flux,

$$\widehat{\mathbf{F}}(v_h)\big|_\epsilon \equiv \begin{cases} \mathbf{F}\big|_{\partial K^+}, & (\mathbf{q}_{\text{e}} \cdot \hat{\mathbf{t}})\big|_{\partial K^+} \geq 0 \\ \mathbf{F}\big|_{\partial K^-}, & \text{otherwise} \end{cases} \qquad \epsilon = \partial K^+ \cap \partial K^- \tag{26}$$

where $\hat{\mathbf{t}}\big|_{\partial K}$ is a unit normal vector of ∂K pointing away from K and ϵ is the interface between two adjacent finite elements K^+ and K^-. An alternative example is the Lax-Friedrichs flux used in Ref. [1],

$$\widehat{\mathbf{F}}(v_h)\big|_\epsilon \equiv \frac{1}{2} \left(\mathbf{F}\big|_{\partial K^+} + \mathbf{F}\big|_{\partial K^-} \right) + \frac{1}{2} \alpha \left[(u\,\hat{\mathbf{t}})\big|_{K^+} + (u\,\hat{\mathbf{t}})\big|_{K^-} \right] \qquad \epsilon = \partial K^+ \cap \partial K^- \tag{27}$$

where the dissipation coefficient α, flux $\mathbf{F}$ and variable u are defined as,

$$\alpha = q_{\text{e}}, \qquad \mathbf{F} = \left\{ \overline{\overline{\mathbf{P}}}^T \cdot \hat{\mathbf{e}}, \ \mathbf{K}, \ \tilde{n}\,\mathbf{q}_{\text{e}}, \ \mathcal{G}\,\mathbf{q}_{\text{e}} \right\}, \qquad u = \{\mathbf{p} \cdot \hat{\mathbf{e}}, \ k, \ \tilde{n}, \ \mathcal{G}\} \tag{28}$$

6

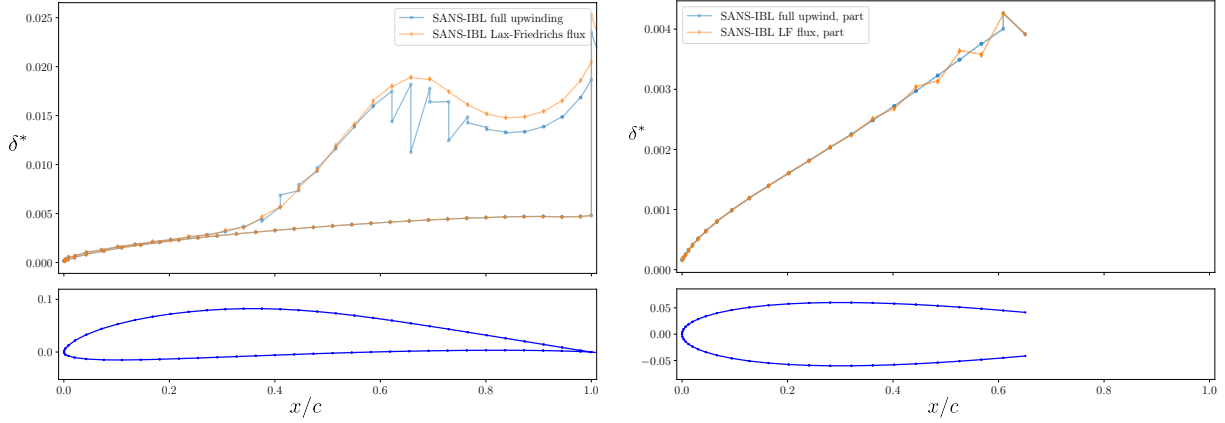**Fig. 2** Left: Eppler 387: $Re = 10^5, \alpha = 4°$. Right: NACA 0012 (segment): $Re = 2 \times 10^5, \alpha = 0°$

However, neither flux choice is sufficiently stable and Fig. 2 illustrates some examples of ill-behaved solution. For a case of transitional flow over the Eppler 387 airfoil, the fully upwinded flux (26) results in excessive jumps in the displacement thickness δ^* at finite element interfaces for the coupled viscous-inviscid solution. In another case of flow over an NACA airfoil segment where forced transition is triggered right before the trailing elements of the segment and the viscous solution is solved with prescribed boundary layer edge velocity (i.e. no viscous-inviscid coupling), the Lax-Friedrichs flux (27) leads to noticeable oscillations in both δ^* and θ.

A fix to the numerical flux problem is identified by investigating the conservation law underlying the IBL momentum equation (5). Based on the derivation of Ref. [1] which covers more details, the momentum conservation law in an integral defect form is,

$$\oint_{\partial\Omega} \left(\overline{\overline{\mathbf{P}}} + \mathbf{q}_e \otimes \mathbf{M}\right) \cdot \hat{\mathbf{t}} + \int_\Omega \left[\frac{\partial \mathbf{M}}{\partial t} - \mathbf{q}_e \left(\rho_e \, \mathbf{q}_e \cdot \hat{\mathbf{n}}_w\right) - \boldsymbol{\tau}_w\right] d\ell = 0 \qquad \forall \Omega \tag{29}$$

which is derived into Eq. (5) by applying the divergence theorem and substituting the wall transpiration term $\rho_e \, \mathbf{q}_e \cdot \hat{\mathbf{n}}_w$ with Eq. (4). The integral defect conservation equation (29) implies that, in lieu of $\overline{\overline{\mathbf{P}}}$, the momentum flux defect $\overline{\overline{\mathbf{J}}} \equiv \overline{\overline{\mathbf{P}}} + \mathbf{q}_e \otimes \mathbf{M}$ needs to be conserved and thus upwinded in the numerical flux definition. To reflect the underlying conservative flux, Eq. (5) is rewritten into an alternative form,

$$\frac{\partial \mathbf{p}}{\partial t} + m \frac{\partial \mathbf{q}_e}{\partial t} + \widetilde{\nabla} \cdot \overline{\overline{\mathbf{J}}} - (\widetilde{\nabla} \cdot \mathbf{M}) \, \mathbf{q}_e - \boldsymbol{\tau}_w = \mathbf{0} \tag{30}$$

the steady-state form of which is discretized using a standard DG formulation,

$$\mathcal{R} \equiv \sum_{K \in \mathcal{T}_h} \int_K \left\{ \mathcal{W} \left[-\mathrm{tr}\left(\overline{\overline{\mathbf{J}}}^T \cdot \left(\widetilde{\nabla}\hat{\mathbf{e}}\right)\right) - (\widetilde{\nabla} \cdot \mathbf{M}) \, \mathbf{q}_e \cdot \hat{\mathbf{e}} - \boldsymbol{\tau}_w \cdot \hat{\mathbf{e}} \right] - \widetilde{\nabla}\mathcal{W} \cdot \overline{\overline{\mathbf{J}}}^T \cdot \hat{\mathbf{e}} \right\} d\ell$$
$$+ \sum_{\partial K \in \partial \mathcal{T}_h} \mathcal{W} \, \hat{\mathbf{t}} \cdot \widehat{\mathbf{F}}_J = 0, \qquad \forall \mathcal{W} \in \mathcal{V}_h \tag{31}$$

At each finite element interface, the flux $\mathbf{F}_J \equiv \overline{\overline{\mathbf{J}}}^T \cdot \hat{\mathbf{e}}$ is replaced with the numerical flux $\widehat{\mathbf{F}}_J$, such as the Lax-Friedrichs form as follows,

$$\widehat{\mathbf{F}}_J(v_h)\big|_\epsilon \equiv \frac{1}{2}\left[\left(\overline{\overline{\mathbf{J}}}^T \cdot \hat{\mathbf{e}}\right)\Big|_{\partial K^+} + \left(\overline{\overline{\mathbf{J}}}^T \cdot \hat{\mathbf{e}}\right)\Big|_{\partial K^-}\right] + \frac{1}{2}\alpha \left[(u\,\hat{\mathbf{t}})\big|_{K^+} + (u\,\hat{\mathbf{t}})\big|_{K^-}\right] \qquad \epsilon = \partial K^+ \cap \partial K^- \tag{32}$$

This DG discretization turns out to fix the aforementioned interface jumps or oscillations in the IBL solution. It is worth noting that Ref. [17] shows the discretization (31) to be dual-inconsistent due to the term $\widetilde{\nabla} \cdot \mathbf{M}$ that involves first derivatives of the solution variable, specifically $\widetilde{\nabla}\delta^*$ in this case. Although dual consistency is not crucial in the current discussion, it plays an important role in the IBL adjoint formulation (to be solved for design optimization or mesh adaptation purposes) and can be recovered with extra modifications [17].

7

Motivated by the fix achieved with the discretization (31), integration by parts on the term involving $\widetilde{\nabla} \cdot \mathbf{M}$ leads to an alternative residual definition,

$$
\begin{aligned}
\mathcal{R} \equiv & \sum_{K \in \mathcal{T}_h} \int_K \left\{ \mathcal{W} \left[-\text{tr}\left(\overline{\overline{\mathbf{P}}}^T \cdot \left(\widetilde{\nabla}\hat{\mathbf{e}}\right)\right) + \hat{\mathbf{e}} \cdot \left(\widetilde{\nabla}\mathbf{q}_e\right) \cdot \mathbf{M} - \boldsymbol{\tau}_w \cdot \hat{\mathbf{e}} \right] - \widetilde{\nabla}\mathcal{W} \cdot \overline{\overline{\mathbf{P}}}^T \cdot \hat{\mathbf{e}} \right\} \, \mathrm{d}\ell \\
& + \sum_{\partial K \in \partial \mathcal{T}_h} \mathcal{W}\, \hat{\mathbf{t}} \cdot [\widehat{\mathbf{F}}_P + \underbrace{(\widehat{\mathbf{F}}_J - \widehat{\mathbf{F}}_P - \mathbf{M} \otimes \mathbf{q}_e \cdot \hat{\mathbf{e}})}_{\text{flux correction}}] = 0, \qquad \forall \mathcal{W} \in \mathcal{V}_h
\end{aligned}
\tag{33}
$$

where $\widehat{\mathbf{F}}_P$ is the numerical flux for $\overline{\overline{\mathbf{P}}}^T \cdot \hat{\mathbf{e}}$. In contrast to the standard DG discretization (25), the discretization (33) of Eq. (5) effectively introduces a correction to the numerical flux based on momentum conservation and fixes the aforementioned issues of solution irregularity.

C. Flow Transition Treatment

The free-transition problem also poses challenges on numerical discretization. First, the transition front is a solution-dependent interface and certain matching conditions need to be satisfied therein such as the turbulent shear stress initial condition (16). One approach to address this problem is a fitted transition treatment which explicitly identifies and parametrizes the interface location. The computational grid can be adapted so that interior cells conform to the identified interface (also known as r-adaptation). Alternatively, sub-cell treatment also exists without modifying the overall grid, such as the cut-cell methods of Refs. [2, 6, 14]). However, both approaches suffers from the interdependence between the viscous solution and the interface topology, which usually adds significant geometric and discretization complexities while compromising the nonlinear solution robustness [14]. Besides, extension to a general unsteady 3D IBL formulation requires considerable implementation efforts.

These drawbacks of the fitted transition approach can be sidestepped by the captured transition treatment which represents the transition front implicitly based on the transition criterion. The turbulent shear stress initial condition (16) at transition is imposed by extending both the amplification factor and the lag equation to the entire domain as in Sec. II. The DG discretization in this work is readily applicable to the captured transition treatment of IBL equations, with trivial extension to 3D and unsteady cases.

Another difficulty of the transition problem is the discontinuity in the IBL equations at the transition front. Such discontinuity arises from disparate laminar and turbulent closure models used for defining the flux $\mathbf{F}$ and source S terms in Eq. (24), and tends to be problematic for numerical discretization and nonlinear solution.

This discontinuity issue is addressed by introducing smoothing effects via a numerical intermittency factor γ, which is defined as,

$$
\gamma(\tilde{n}, s) = \begin{cases} 0, & f \in (-\infty, -1] \\ \dfrac{1}{2}\left[1 + \sin\left(\dfrac{\pi f}{2}\right)\right], & f \in (-1, 1) \\ 1, & f \in [1, +\infty) \end{cases} \qquad f = \max\left\{ \frac{\tilde{n} - \tilde{n}_{\text{crit}}}{\varDelta \tilde{n}}, \frac{s - s_{\text{trip}}}{\varDelta s} \right\}
\tag{34}
$$

As the boundary layer transitions, the value γ varies continuously between $\gamma = 0$ and $\gamma = 1$ which correspond to fully laminar and turbulent flows respectively. In the definition (34), the function s is a signed geodesic (surface) distance with respect to the prescribed trip location s_{trip}, and $\varDelta s$ models the length scale of the transitional region, which is currently chosen to be twice the local grid cell length scale that is fixed a priori. For the natural transition region to span a consistent length, the parameter $\varDelta \tilde{n}$ is chosen as,

$$
\varDelta \tilde{n} = \varDelta s \, \frac{\mathbf{q}_e \cdot \widetilde{\nabla}\tilde{n}}{q_e} \approx \frac{\varDelta s \, f_N}{\theta}
\tag{35}
$$

where the turbulent f_N given in Eq. (11) is used.

Then, the flux $\mathbf{F}$ and source S terms in the generic equation (24) are defined as linear combinations of laminar and turbulent components weighted by γ,

$$
\mathbf{F} = (1 - \gamma)\mathbf{F}_{\text{L}} + \gamma \mathbf{F}_{\text{T}}, \qquad S = (1 - \gamma)S_{\text{L}} + \gamma S_{\text{T}}
\tag{36}
$$

where the subscripts "L" and "T" indicate laminar and turbulent definitions respectively and the intermittency factor γ conceptually characterizes the fraction of turbulent contribution to the overall IBL equations. With the definition (36),

the DG discretization in Eqs. (25) and (33) is directly applicable to flow transition problems and free of discontinuity due to different laminar and turbulent closures. In the current work, the artificial construction of γ is solely intended for numerical regularization, whereas the physical modeling of intermittency phenomena in turbulent flows deserves a dedicated separate discussion and is not considered here.

IV. Strongly-coupled Viscous-Inviscid Solution

A. Viscous Inviscid Interaction

The viscous-inviscid interaction scheme of Ref. [1] is adopted here to achieve strong coupling and allow for a flexible choice of the inviscid flow solver. Table 1 summarizes components of the current viscous-inviscid interaction formulation.

Table 1   List of abbreviations, variables, residuals and governing equations in the coupled global system

Abbreviation	Unknown Q	Residual $\mathcal{R}$	Governing Equation
IBL	$\delta^*, \theta, \tilde{n}, \mathcal{G}$	2D IBL	(5), (6), (9), (14)/(17)
inv	Φ	Inviscid	(37)
auxi	Λ	Auxiliary inviscid	(38)
auxv	$\mathbf{q}_e$	Auxiliary viscous	(39)

As an example, the current work considers steady-state incompressible flows, for which the inviscid flow field is governed by the following equation,

$$\nabla^2 \Phi = 0 \qquad \text{subject to} \qquad (\rho_i \, \mathbf{q}_i)_w \cdot \hat{\mathbf{n}}_w = \Lambda \quad \text{(boundary condition)} \tag{37}$$

and solved by a vorticity-and-source-based panel method [1]. Here, Φ is the unknown velocity potential and the flow velocity is $\mathbf{q}_i = \nabla \Phi$. The source term Λ models the displacement effect originating from viscous-inviscid interaction, geometry deformation or wall blowing/suction.

The coupling between viscous and inviscid solutions is realized through additional auxiliary equations,

$$\Lambda - \widetilde{\nabla} \cdot \mathbf{M} = 0 \tag{38}$$
$$\mathbf{q}_e - \mathbf{q}_i = 0 \tag{39}$$

where Λ and $\mathbf{q}_e$ are the auxiliary variables. The mass defect flux $\mathbf{M} = \rho_e \, \delta_1^* \, \mathbf{q}_e$ depends the IBL solution and the auxiliary variable $\mathbf{q}_e$. The inviscid flow velocity $\mathbf{q}_i$ is governed by the inviscid flow as $\mathbf{q}_i = \nabla \Phi$. The auxiliary equations (38) and (39) are discretized as L_2 projections onto the auxiliary variables Λ and $\mathbf{q}_e$, which are approximated with piecewise-constant and piecewise-linear DG basis functions respectively [1].

B. Global Newton Solution Method

To ensure robust viscous-inviscid interactive solution, the following global coupled system of equations are solved simultaneously,

$$\mathcal{R}(\boldsymbol{Q}) = \mathbf{0}, \qquad \mathcal{R} \equiv \begin{pmatrix} \mathcal{R}_{\text{auxv}}(Q_{\text{auxv}}, Q_{\text{inv}}) \\ \mathcal{R}_{\text{auxi}}(Q_{\text{auxv}}, Q_{\text{auxi}}, Q_{\text{IBL}}) \\ \mathcal{R}_{\text{IBL}}(Q_{\text{auxv}}, Q_{\text{IBL}}) \\ \mathcal{R}_{\text{inv}}(Q_{\text{auxi}}, Q_{\text{inv}}) \end{pmatrix}, \qquad \boldsymbol{Q} \equiv \begin{pmatrix} Q_{\text{auxv}} \\ Q_{\text{auxi}} \\ Q_{\text{IBL}} \\ Q_{\text{inv}} \end{pmatrix} \tag{40}$$

9

where $\mathcal{R}$ and Q denote the global residual and solution respectively, with their components summarized in Table 1. The viscous-inviscid interaction is manifested in the structure of the jacobian of the global residual,

$$\left[\frac{\partial \mathcal{R}}{\partial Q}\right] = \begin{pmatrix} \left[\frac{\partial \mathcal{R}_{\text{auxv}}}{\partial Q_{\text{auxv}}}\right] & 0 & 0 & \left[\frac{\partial \mathcal{R}_{\text{auxv}}}{\partial Q_{\text{inv}}}\right] \\ \left[\frac{\partial \mathcal{R}_{\text{auxi}}}{\partial Q_{\text{auxv}}}\right] & \left[\frac{\partial \mathcal{R}_{\text{auxi}}}{\partial Q_{\text{auxi}}}\right] & \left[\frac{\partial \mathcal{R}_{\text{auxi}}}{\partial Q_{\text{IBL}}}\right] & 0 \\ \left[\frac{\partial \mathcal{R}_{\text{IBL}}}{\partial Q_{\text{auxv}}}\right] & 0 & \left[\frac{\partial \mathcal{R}_{\text{IBL}}}{\partial Q_{\text{IBL}}}\right] & 0 \\ 0 & \left[\frac{\partial \mathcal{R}_{\text{inv}}}{\partial Q_{\text{auxi}}}\right] & 0 & \left[\frac{\partial \mathcal{R}_{\text{inv}}}{\partial Q_{\text{inv}}}\right] \end{pmatrix} \tag{41}$$

where the lower-right 2-by-2 submatrix is invariably block-diagonal by design to avoid intrusive interdependence between viscous and inviscid solvers.

Similar to Ref. [14], a Newton method is employed to solve the nonlinear system. The n-th Newton solution update is,

$$\mathcal{R}(Q^n) + \left[\frac{\partial \mathcal{R}}{\partial Q}\right]^n \Delta Q^n = \mathbf{0} \tag{42}$$

$$Q^{n+1} = Q^n + \Delta Q^n \tag{43}$$

The linear system (42) is solved for the solution update ΔQ using a generic direct linear solver (specifically, LU factorization with partial column pivoting) available in the UMFPACK library [18] and an initial solution guess Q^0 is provided for the Newton update to start with.

Nonlinear solution robustness is enhanced using a linear-search algorithm [14] and pseudo-transient continuation (PTC) [19]. In the PTC extension, only the IBL equations $\mathcal{R}_{\text{IBL}}$ are augmented with unsteady terms while the other equations remain unchanged. The current captured transition treatment is conducive to linear-search and PTC extensions. In comparison, the fitted transition approach in Refs. [2, 6, 14] has to resort to under-relaxation for the Newton method which compromises the robustness to some extent and precludes straightforward application to unsteady problems.

V. Viscous Analysis Examples

The proposed IBL method is implemented in the Solution Adaptive Numerical Simulator (SANS) code base [19] and denoted as SANS-IBL in the following discussion. This method is exercised on representative airfoil test cases and compared with XFOIL [15], an established tool for airfoil analysis with an IBL viscous formulation.

A. Eppler 387

The first test case is on an incompressible flow over the Eppler 387 airfoil at angle of attack $\alpha = 4°$ and chord-based Reynolds number $Re = 10^5$. It features a separation bubble and ensuing flow transition on the suction side (i.e. upper surface) of the airfoil. A sample configuration is illustrated in Fig. 3, where the wake geometry and mesh are generated from XFOIL based on the inviscid flow velocity field. For all the numerical results of this and the following test cases, the SANS-IBL method uses a polynomial order $p = 1$ and the Lax-Friedrichs numerical flux for the DG discretization. The weighted integrals in the DG weak form are integrated using a three-point Gauss-Legendre quadrature rule for computational efficiency, while higher-order quadrature that is trialed (namely, the seven-point and twenty-point rules) has negligible impact on the solution.

Fig. 4 illustrates a close match between numerical results of SANS-IBL and XFOIL. The comparison also includes a 3D axisymmetric IBL formulation MTFLOW [20], which adopts a captured transition approach for free transition modeling. The MTFLOW results are obtained from a ring wing geometry with a radius-to-chord ratio of 100 in order to produce approximately 2D flows at any airfoil cross section. In view of the difference in far-field boundary conditions, the angle of attack in MTFLOW is adjusted to match XFOIL's lift coefficient. Compared to XFOIL and SANS-IBL as shown in Fig. 4, the pressure gradient at reattachment after the separation bubble is less steep in MTFLOW and
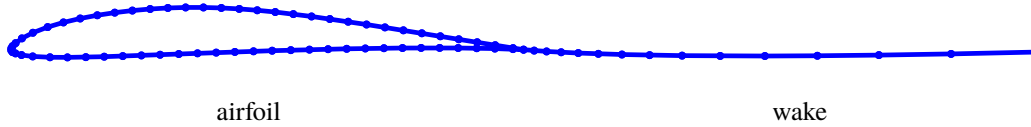
airfoil   wake

Fig. 3   Sample grid of Eppler 387 airfoil test case $\alpha = 4°$ **(64 and 14 elements on the airfoil and the wake respectively)**

implies a coarser transition resolution. This is mainly attributed to the fact that MTFLOW imposes a constant shear stress level $(c_\tau)_{T,\ init}$ at the turbulence onset, which tends to be much smaller than the solution-dependent empirical value in Eq. (16). On the other hand, enforcing the interface condition in Eq. (16) in MTFLOW is nontrivial because the the amplification factor growth and the lag equations are solved as a single equation with a shared variable $\mathcal{G}$ (similar to the captured transition treatment of Ref. [14]).

That difficulty is overcome by the current captured transition treatment of SANS-IBL. The intermittency factor γ of SANS-IBL as shown in Fig. 5 illustrates a transitional region, identified by $0 < \gamma < 1$, that spans only a handful of (e.g. three) elements, and achieves a comparable transition resolution as XFOIL. Also, it provides sufficient numerical regularization for the otherwise discontinuous IBL equations at flow transition that are not readily amenable to the nonlinear solver. In addition, by defining the transition length scale Δs to be proportional to a representative grid element size, the resolution of the transition region is further sharpened with mesh refinement.

B. FK67-K-170

A second stress test is provided by the FX67-K-170 sailplane airfoil at Reynolds number 2×10^6. For angle of attack $\alpha = 4.156°$, the incompressible flow over the FX67-K-170 airfoil features small yet intense separation bubbles and correspondingly induced flow transition. Such characteristics need to be well resolved in order to predict the drag accurately and are thus quite demanding for the numerical method. Fig. 6 shows sample numerical results of SANS-IBL that match the XFOIL results closely.

At the same flow condition, a grid refinement study is also conduct for both SANS-IBL and XFOIL, the results of which are shown in Fig. 7. The study reveals noticeable oscillation in the drag coefficient computed from XFOIL as its mean trend line converges gradually with grid refinement. This observation is consistent with the findings reported in Ref. [2] and the issue is attributed to the fitted transition treatment based on a cut-cell method. Although the true location of the transition points remains invariant, the cut cell configuration changes from grid to grid (as it is refined) in order to numerically track the transition front, and turns out to have a strong bearing on the resulting viscous solution. Such grid sensitivity often requires excessive grid resolution to provide reliably converged solution. In contrast, the SANS-IBL method with a captured transition treatment demonstrates an unambiguous trend of grid convergence in its numerical solution as illustrated in Fig. 7, which is more favorable.

Fig. 8 shows the drag polars at $Re = 2 \times 10^6$ computed from SANS-IBL and XFOIL on three different grids (with respectively 160, 240 and 320 elements on the airfoil surface). The comparison demonstrates an overall reasonable agreement between SANS-IBL and XFOIL. It is also worth noting that, as highlighted in Fig. 9, the drag polar computed from XFOIL appears more ragged than SANS-IBL as the angle of attack traverses the range of $0° < \alpha < 5°$. For this range of α, the separation bubbles are strong and the corresponding transition front moves across nodes on a given fixed grid. The resulting wavy behavior in the drag polar is another manifestation of the solution sensitivity to the underlying cut-cell fitted transition treatment. Such behavior will lead to unreliable derivative calculations, e.g. $\partial(c_d)/\partial\alpha$ and $\partial(c_d)/\partial(c_l)$, and hence is not desirable, for example, in the context of design optimization. In comparison, that problem is sidestepped in the SANS-IBL method which is able to compute a smooth drag polar.

VI. Conclusions

A strongly coupled IBL method with DG finite element discretization is presented. In place of the fitted transition treatment, a captured transition approach is proposed that generalizes to the 3D case more conveniently and leverages more robust nonlinear solution techniques such as line search and pseudo-transient continuation (PTC). Also, numerical flux correction to the standard DG discretization is introduced in accordance with the underlying conservation law and to regularize otherwise ill-behaved solutions. Numerical results compared to XFOIL demonstrate the comparable flow transition resolution and more favorable grid/parameter insensitivity of the proposed method, which makes it suitable
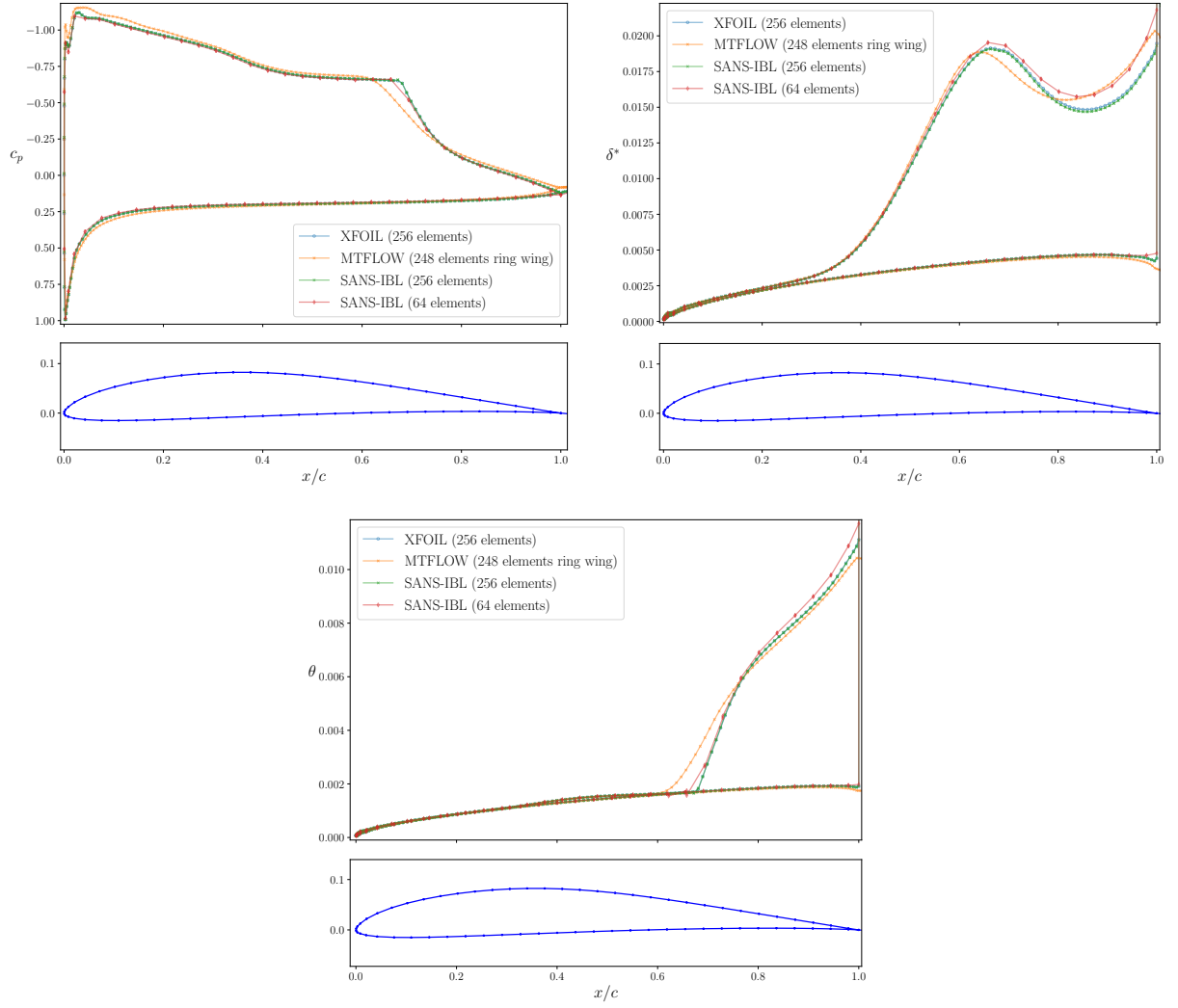
Fig. 4   Eppler 387, $\alpha = 4°$, $Re = 10^5$: pressure coefficient c_p (upper left), displacement thickness δ^* (upper right) and momentum thickness θ (lower center)
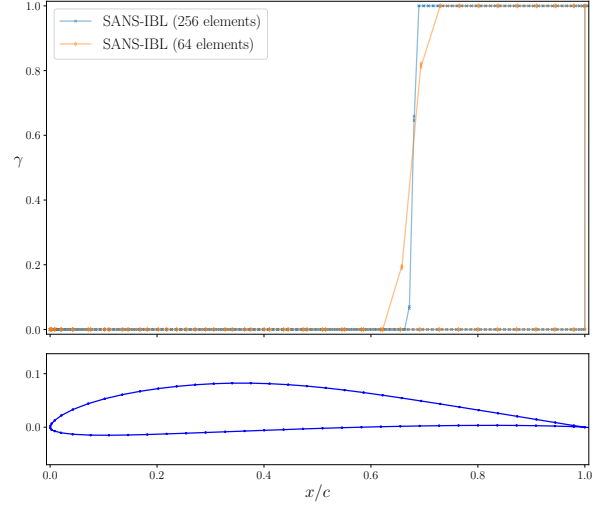
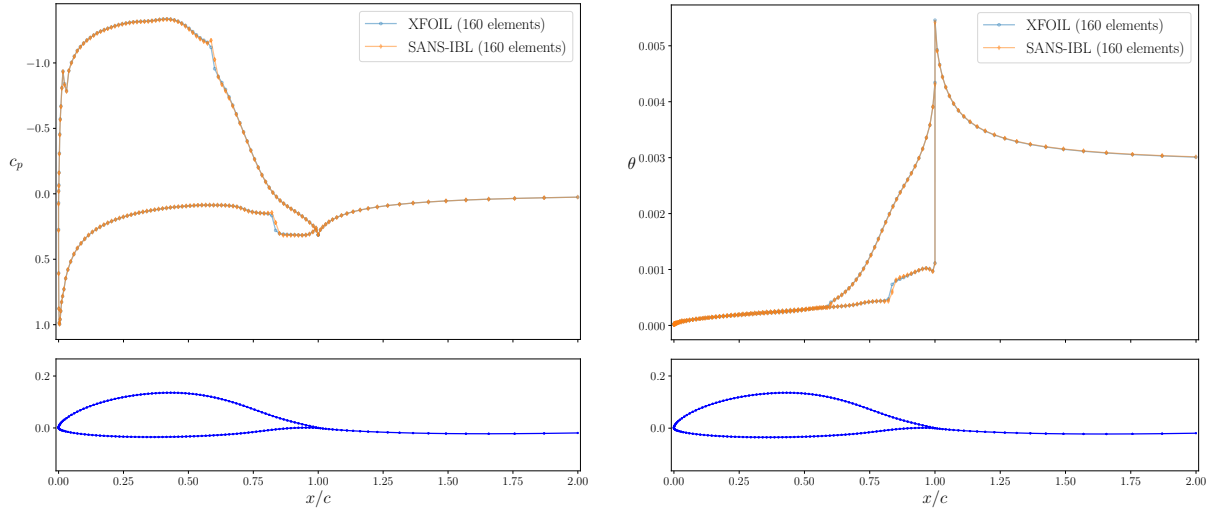**Fig. 5   Intermittency factor γ of SANS-IBL solution for different mesh resolutions**

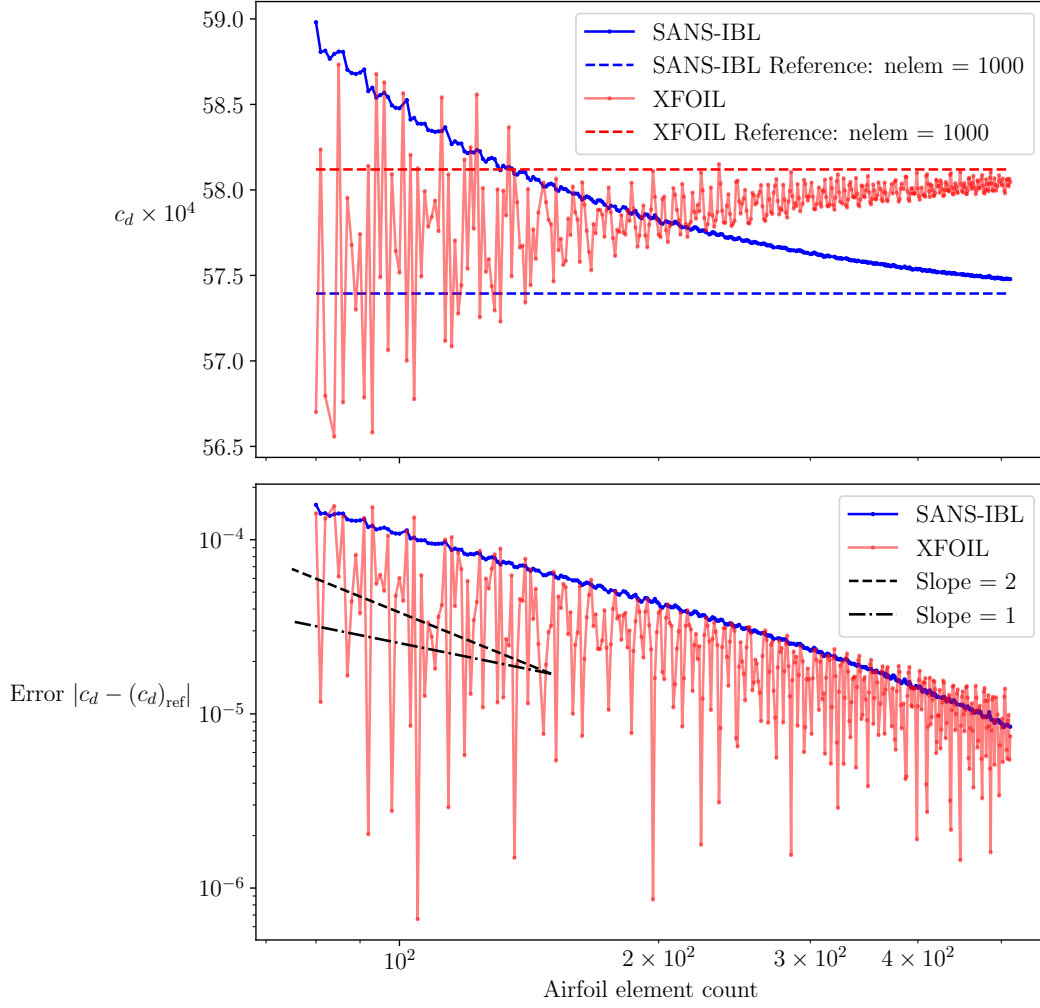**Fig. 6   FX67-K-170,** $\alpha = 4.156°, Re = 2 \times 10^6$**: pressure coefficient c_p (left) and momentum thickness θ (right)**
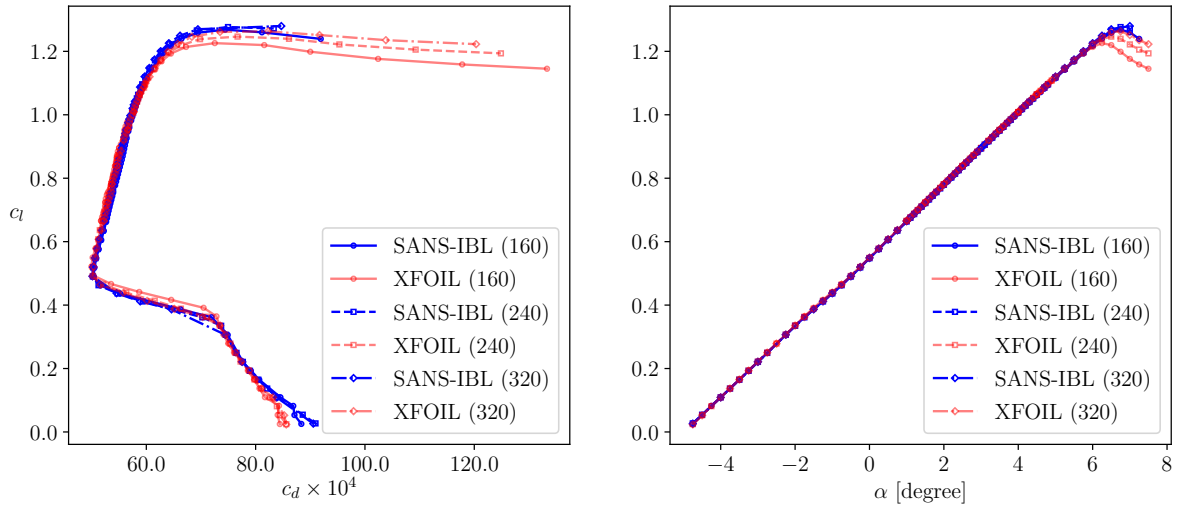
13

Fig. 7   Grid convergence of drag coefficient c_d.

Fig. 8   Drag polar for FX67-K-170 airfoil at $Re = 2 \times 10^6$ for different grid refinement levels. (Airfoil element count indicated in parentheses)
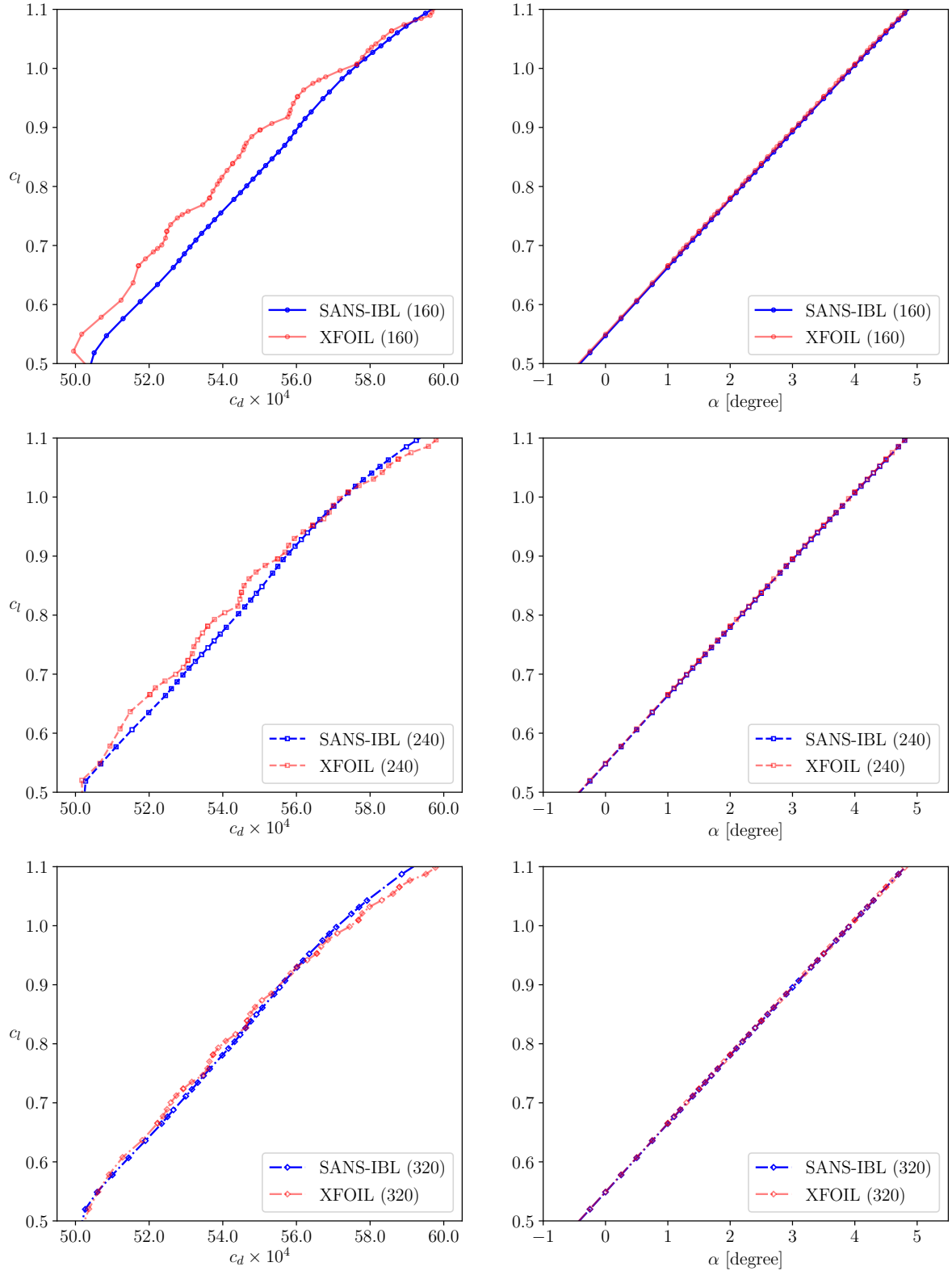
Fig. 9 Zoom-in views of drag polar for FX67-K-170 airfoil at $Re = 2 \times 10^6$ **for different grid refinement levels. (Airfoil element count indicated in parentheses)**

for practical viscous aerodynamic analysis with free transition. Future development will focus on applying the current method to a fully 3D IBL formulation.

Acknowledgments

References

[1] Zhang, S., "A Non-parametric Discontinuous Galerkin Formulation of the Integral Boundary Layer Equations with Strong Viscous-Inviscid Coupling," Master's Thesis, Massachusetts Institute of Technology, Feb. 2018.

[2] Drela, M., "XFOIL: An Analysis and Design System for Low Reynolds Number Airfoils," *Low Reynolds number aerodynamics*, Vol. 54, 1989, pp. 1–12. doi:10.1007/978-3-642-84010-4_1, URL http://link.springer.com/chapter/10.1007/978-3-642-84010-4_1.

[3] Morgado, J., Vizinho, R., Silvestre, M., and Páscoa, J., "XFOIL vs CFD performance predictions for high lift low Reynolds number airfoils," *Aerospace Science and Technology*, Vol. 52, 2016, pp. 207–214. doi:10.1016/j.ast.2016.02.031, URL https://linkinghub.elsevier.com/retrieve/pii/S1270963816300839.

[4] Drela, M., *Flight Vehicle Aerodynamics*, The MIT Press, Cambridge, MA, USA, 2014.

[5] Martins, J. R., Kenway, G. K. W., and Brooks, T., "Multidisciplinary Design Optimization of Aircraft Configurations Part 2: High-fidelity Aerostructural Optimization," , May 2016. URL http://mdolab.engin.umich.edu, lecture series, Von Karman Institute for Fluid Dynamics, Sint-Genesius-Rode, Belgium.

[6] Drela, M., and Giles, M. B., "Viscous-inviscid Analysis of Transonic and Low Reynolds Number Airfoils," *AIAA Journal*, Vol. 25, No. 10, 1987, pp. 1347–1355. doi:10.2514/3.9789, URL http://arc.aiaa.org/doi/abs/10.2514/3.9789.

[7] Bieterman, M., Melvin, R., Johnson, F., Bussoletti, J., Young, D., Huffman, W., Hilmes, C., and Drela, M., "Boundary Layer Coupling in a General Configuration Full Potential Code," Tech. rep., The Boeing Company, 1994.

[8] Johnson, F. T., Tinoco, E. N., and Yu, N. J., "Thirty Years of Development and Application of CFD at Boeing Commercial Airplanes, Seattle," *Computers & Fluids*, Vol. 34, No. 10, 2005, pp. 1115–1151. doi:10.1016/j.compfluid.2004.06.005, URL http://linkinghub.elsevier.com/retrieve/pii/S0045793005000125.

[9] Young, D. P., Melvin, R. G., Huffman, W. P., Arian, E., Hong, M., and Drela, M., "Implementation of a Separated Flow Capability in TRANAIR," *AIAA Journal*, Vol. 52, No. 8, 2014, pp. 1699–1716. doi:10.2514/1.J052646, URL http://arc.aiaa.org/doi/10.2514/1.J052646.

[10] Nishida, B. A., "Fully Simultaneous Coupling of the Full Potential Equation and the Integral Boundary Layer Equations in Three Dimensions," Ph.D. Thesis, Massachusetts Institute of Technology, 1996.

[11] Mughal, B. H., "Integral Methods for Three-Dimensional Boundary Layers," Ph.D. Thesis, Massachusetts Institute of Technology, 1998.

[12] Drela, M., "Three-Dimensional Integral Boundary Layer Formulation for General Configurations," *21st AIAA Computational Fluid Dynamics Conference*, American Institute of Aeronautics and Astronautics, San Diego, CA, 2013. doi:10.2514/6.2013-2437, URL http://arc.aiaa.org/doi/pdf/10.2514/6.2013-2437.

[13] Zhang, S., Galbraith, M., Allmaras, S., Drela, M., and Darmofal, D., "A Non-parametric Discontinuous Galerkin Formulation of the Integral Boundary Layer Equations With Strong Viscous/Inviscid Coupling," *23rd AIAA Computational Fluid Dynamics Conference, 2017 AIAA Aviation and Aeronautics Forum and Exposition*, American Institute of Aeronautics and Astronautics, Denver, Colorado, 2017.

[14] Zhang, S., Drela, M., Allmaras, S. R., Galbraith, M. C., and Darmofal, D. L., "A Strongly-coupled Non-parametric Integral Boundary Layer Method for Aerodynamic Analysis with Free Transition," *AIAA Scitech 2019 Forum*, American Institute of Aeronautics and Astronautics, San Diego, CA, 2019. doi:10.2514/6.2019-1154, URL https://arc.aiaa.org/doi/10.2514/6.2019-1154.

[15] Drela, M., "XFOIL: Subsonic Airfoil Development System, (version 6.99)," , Dec. 23, 2013. URL http://web.mit.edu/drela/Public/web/xfoil/, Available at http://web.mit.edu/drela/Public/web/xfoil/. Retrieved on December 6, 2017 .

[16] Drela, M., "MISES Implementation of Modified Abu-Ghannam/Shaw Transition Criterion (Second Revision)," Tech. rep., 1998.

[17] Oliver, T. A., and Darmofal, D. L., "Analysis of Dual Consistency for Discontinuous Galerkin Discretizations of Source Terms," *SIAM Journal on Numerical Analysis*, Vol. 47, No. 5, 2009, pp. 3507–3525. doi:10.1137/080721467, URL http://epubs.siam.org/doi/abs/10.1137/080721467.

[18] Davis, T. A., "Algorithm 832: UMFPACK V4.3–An Unsymmetric-pattern Multifrontal Method," *ACM Transactions on Mathematical Software*, Vol. 30, No. 2, 2004, pp. 196–199. doi:10.1145/992200.992206, URL http://portal.acm.org/citation.cfm?doid=992200.992206.

[19] Galbraith, M. C., Allmaras, S. R., and Darmofal, D. L., "SANS RANS solutions for 3D benchmark configurations," *2018 AIAA Aerospace Sciences Meeting*, American Institute of Aeronautics and Astronautics, Reston, Virginia, 2018. doi:10.2514/6.2018-1570, URL https://arc.aiaa.org/doi/10.2514/6.2018-1570.

[20] Drela, M., "MTFLOW Overview," , November 2015. URL http://web.mit.edu/drela/Public/web/mtflow/.